Review Article: Rare-earth monosulfides as durable and efficient cold cathodes[a)]

Marc Cahay[b)] and Punit Boolchand
School of Electronic and Computing Systems, University of Cincinnati, Cincinnati, Ohio 45221

Steven B. Fairchild and Larry Grazulis
Air Force Research Laboratory, Materials and Manufacturing Directorate, AFRL/RXPS, Wright-Patterson AFB, Ohio 45433

Paul T. Murray
Research Institute, University of Dayton, Dayton, Ohio 45469

Tyson C. Back
Universal Technology Corporation, 1270 N. Fairfield Rd, Dayton, Ohio 45432

Vincent Semet and Vu Thien Binh
Equipe Emission Electronique, LPMCN, University of Lyon 1, Villeurbanne 69622, France

Xiaohua Wu, Daniel Poitras, and David J. Lockwood
Institute for Microstructural Sciences, National Research Council, Ottawa, Ontario K1A OR6, Canada

Fei Yu and Vikram Kuppa
School of Energy, Environmental, Biological, and Medical Engineering, University of Cincinnati, Cincinnati, Ohio 45221

In their rocksalt structure, rare-earth monosulfides offer a more stable alternative to alkali metals to attain low or negative electron affinity when deposited on various III-V and II-VI semiconductor surfaces. In this article, the authors first describe the successful deposition of lanthanum monosulfide via pulsed laser deposition on Si and MgO substrates. These thin films have been characterized by x-ray diffraction, atomic force microscopy, high resolution transmission electron microscopy, ellipsometry, Raman spectroscopy, ultraviolet photoelectron spectroscopy, and Kelvin probe measurements. For both LaS/Si and LaS/MgO thin films, the effective work function of the submicron thick thin films was determined to be about 1 eV from field emission measurements using the scanning anode field emission microscopy technique. The physical reasons for these highly desirable low work function properties were explained using a patchwork field emission model of the emitting surface. In this model, nanocrystals of low work function materials having a $\langle 100 \rangle$ orientation perpendicular to the surface and outcropping it are surrounded by a matrix of amorphous materials with a higher work function. To date, LaS thin films have been used successfully as cold cathode emitters with measured emitted current densities as high as 50 A/cm^2. Finally, we describe the successful growth of LaS thin films on InP substrates and, more recently, the production of LaS nanoballs and nanoclusters using pulsed laser ablation. © *2011 American Vacuum Society*. [DOI: 10.1116/1.3653275]

I. INTRODUCTION

Typically, low work function surfaces are generally highly chemically reactive. As a result, cold cathodes made of these materials are very unstable. Beginning in 2001, we have studied rare-earth (RE) monosulfide bulk samples and thin films for use in the development of a new class of field emitters that turned out to be very reliable and durable.[1–4] Rare earth compounds do not suffer from all the limitations of cesiated surfaces. A summary of some of the material properties of RE monosulfides in their rocksalt cubic form is given in Table I. When extrapolated from high-temperature measurements,[5] the work function (WF) of these compounds is predicted to be quite small at room temperature (around

1 eV). It is therefore expected that these materials can be used to reach negative electron affinity (NEA) when deposited on p-type doped semiconductors. For instance, LaS has a lattice constant (5.854 Å) very close to the lattice constant of InP (5.8688 Å) and NdS has a lattice constant (5.69 Å) very close to the lattice constant of GaAs (5.6533 Å). Since the room temperature WFs of LaS (1.14 eV) and NdS (1.36 eV) are, respectively, below the band gap of InP (1.35 eV) and GaAs (1.41 eV), NEA can therefore be reached at InP/LaS and GaAs/NdS interfaces using heavily p-type doped semiconductors. Recently, we confirmed this result by means of a first-principle electronic-structure method based on a local-density approximation to density-functional theory.[6] This analysis predicted a 0.9 and 1.1 eV WF for LaS[7] and NdS,[8] respectively, at low temperature. Two other important features of the face-centered-cubic form of the rare-earth compounds listed in Table I are the

---

TABLE I. Materials parameters of some sulfides of rare-earth metals (cubic form): a (lattice constant in Å), WF (work function at room temperature), T_m (melting point in °C), and ρ, electrical resistivity (in $\mu\Omega$ cm)[5]. [Reprinted with permission from O. Eriksson, M. Cahay, and J. Wills, Phys. Rev. B **65**, 033304 (2002).]

ErS	YS	NdS	GdS	PrS	CeS	LaS	EuS	SmS
a (Å) 5.424	5.466	5.69	5.74	5.747	5.778	5.854	5.968	5.970
W (eV)		1.36		1.26	1.05	1.14		
T_m (°C)	2060	2200		2230	2450	2200		1870
ρ ($\mu\Omega$ cm)		242		240	170	25		

fairly large melting temperature (about 2000 °C) and their fairly good electrical resistivity (a few tens of $\mu\Omega$ cm).

Our work was motivated by the original proposal by Walter Friz for an InP/CdS/LaS cold cathode emitter concept, which we refer to hereafter as the *Friz cathode*.[9] The architecture of the structure is shown in Fig. 1. A schematic energy band diagram along the growth direction throughout the proposed structure is shown in Fig. 2. The main elements in the design and functioning of such an emitter are: (1) a wide bandgap semiconductor slab equipped on one side with a heavily doped n-type InP substrate that supplies electrons at a sufficient rate into the conduction band, and (2) on the opposite side, a thin semimetallic LaS film that facilitates the coherent transport (tunneling) of electrons from the semiconductor conduction band into vacuum. As shown in Fig. 1, an array of Au contacts is defined on the surface of the LaS thin film to bias the structure. The bias is applied between the InP substrate and the metal grid with emission occurring from the exposed LaS surface.

In the Friz cathode, the choice of a LaS semimetallic thin film grown on nominally undoped CdS is quite appropriate since the lattice constant of CdS (5.83 Å) is very close to the lattice constant of LaS (5.85 Å) in its cubic crystalline form. Additionally, LaS is expected to have quite a low temperature work function (1.14 eV),[5] a feature which, when combined with the large energy gap (2.5 eV) of CdS leads to the
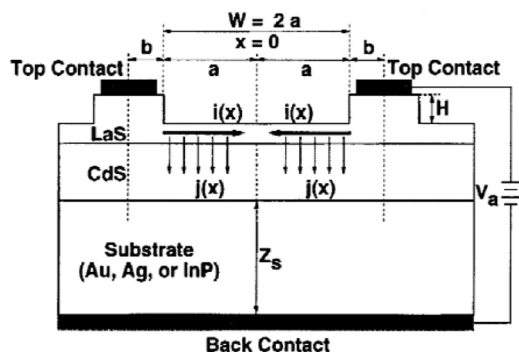

FIG. 1. Cross-section of the Friz cold cathode, which consists of an electron emitter (Au, Ag, or heavily doped InP substrate), a tens of nanometers thick wide-bandgap (2.4 eV) CdS layer, and a LaS thin film on the surface. The NEA at the CdS/LaS interface facilitates the injection of electrons into vacuum. The top emitting surface is biased with an array of emitter fingers. [Reprinted with permission from P. D. Mumford and M. Cahay, Journal of Applied Physics **81**, 3707 (1997).]
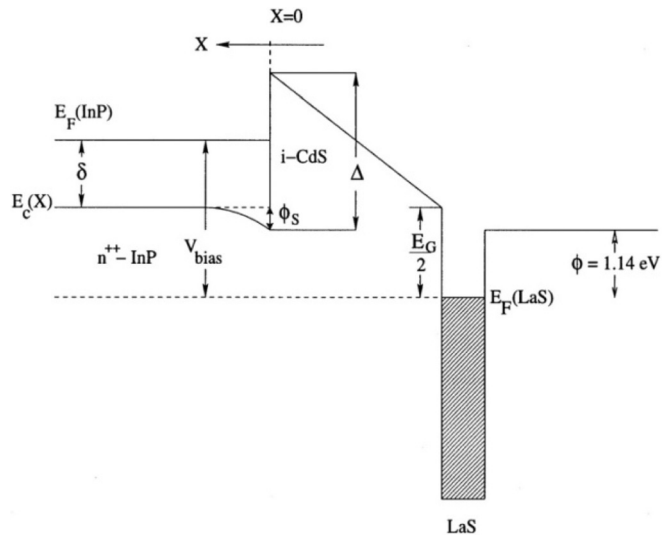
FIG. 2. Energy band diagram across the Friz cathode from the substrate into vacuum. The substrate is held at ground potential and a positive bias is applied on the LaS thin film using the array of emitter fingers shown in Fig. 1

NEA of the semiconductor material. In fact, we have studied the electronic structure of the CdS/LaS interface by means of a first-principles electronic-structure method based on a local-density approximation to density-functional theory.[7] The extrapolated 1.14 eV low work function of LaS was reproduced by that theory. It was found that NaCl structured layers of LaS should grow in an epitaxial way on a CdS substrate with a ZnS structure.[7]

In 1996, Mumford and Cahay modeled the Friz cathode and showed that with a small forward bias (<20 V), some of the electrons originating from the InP substrate and tunneling through the CdS layer are captured in the LaS thin film, eventually leading to an effective reduction in the semimetallic thin film.[10] This leads to a substantial increase in the Friz cathode emission current. Current densities of several 100 A/cm^2 could be achieved with this cathode. With enough forward bias on the emitter fingers, electrons emitted from the InP substrate tunnel through the CdS layer and are emitted into vacuum as a result of the NEA at the CdS/LaS interface. However, there can be partial trapping of electrons by the LaS semimetallic thin film, which can lead to a lateral current flow and current crowding[11,12] and self-heating effects[13] in the cathode.

This paper is organized as follows. We first review our preliminary work on making LaS targets and the growth of LaS thin films on Si and MgO substrates using pulsed laser deposition (PLD). Various characterization tools were used to study the LaS thin films including: x-ray diffraction (XRD), atomic force microscopy (AFM), high resolution transmission electron microscopy (HRTEM), Raman spectroscopy, and ellipsometry. The thin film WF was determined *in situ* by ultraviolet photoelectron spectroscopy (UPS) and compared with the results of Kelvin probe (KP) measurements in air. These WF values was compared to the results for the effective WF values extracted from the field emission (FE) of the thin films recorded using scanning anode field emission

microscopy (SAFEM). The low effective WF ($\sim$1 eV) of the films was interpreted in terms of a recently developed patchwork FE model of the emitting surface. The main ingredients of the patchwork FE model and its practical implications are emphasized. Finally, we describe the successful growth of LaS thin films on InP substrates and, more recently, the production of LaS nanoballs and nanoclusters using pulsed laser ablation (PLA).

II. EXPERIMENT

In our PLD experiments[1–4] the target to substrate distance was set equal to about 10 cm and the vacuum chamber base pressure was typically a few 10^{-8} Torr. A pulsed Lambda Physik LPX 305 excimer laser operating at a wavelength of 248 nm and a repetition rate up to 10 Hz was used for the deposition. The beam spot size on target was about 4×8 mm^2 and the laser energy was estimated to be between 300 and 400 mJ/pulse. During deposition, the target was rotated on axis while galvanometers were used to raster the laser beam in a uniformly random pattern over the surface of the target. This configuration produces a uniform laser plume by preventing the uneven erosion of the target.

The XRD 2Θ scans were performed using a PanAlytical X'Pert Pro x-ray diffraction system in which the incident angle was set equal to 5°. Surface images were obtained by AFM using a Pacific Nanotechnology Nano-R SPM (model no. 0-200-002) operating in vibrating mode. Line scans were performed to measure the surface roughness and the grain size of the films was extracted using the Scherrer formula.[14]

The LaS films were characterized with a Staib multitechnique surface analysis system equipped with a DESA 150 double-pass cylindrical mirror analyzer. The background pressure in the system was 3×10^{-10} Torr. The binding energy scale was calibrated against the Fermi edge of a sputter cleaned Au sample. The UPS data were acquired using the Specs 10/35 He I (21.22 eV) gas discharge lamp. Resolution was determined from the width of the Au Fermi edge, which was found to be 250 meV. The sample was negatively biased in order to determine the true work function of the sample. The WF of the thin films was also measured *in situ* using a McCallister KP-6500 Kelvin probe with a stainless steel tip with a 5 mm diameter. The procedure involved first determining the WF of the tip using UPS. The WF tip value was found to be 4.8 eV. The absolute value of the film WF was then determined by the difference between the KP tip and the sample as recorded in the KP experiments.

A variable-angle spectroscopic ellipsometer (VASE, J.A. Woollam Co. Lincoln, NE) was used for the characterization of the optical constants of the film in the near UV and visible wavelength range.

To investigate the crystalline texture of the films, a $\langle 011 \rangle$ cross-section TEM sample was prepared following standard procedures. Two bars were cut out of a wafer, and were glued together with the film sides face-to-face to make the central part of a 3 mm diameter cross-section disc. Then the disc was mechanically thinned to a thickness of $\sim$100 μm. The thinned disc was dimpled from both sides with 3 μm dia-

mond paste until the center of the disc was $\sim$20 μm thick, and then polished from both sides with 1 μm diamond paste to obtain a very smooth surface. The final thinning until perforation was conducted using Ar ion-milling from both sides using an ion beam angle of 8°, and a gun voltage of 6 kV. The TEM sample was examined in a Philips EM430T operating at 250 kV.

The SAFEM technique was used to measure the current-voltage (I-V) characteristics at different surface locations and at different temperatures of a LaS thin film with an area of about a 1 cm. For one location, the full set of measured I-V characteristics (total measured current versus applied voltage) for different values of Z, the distance between the cathode surface and the probe ball, were then analyzed in order to extract the current density, J, versus the actual applied field, F (J-F) data.[15,16]

Raman measurements were performed at 295 K employing 1 mW of 488 nm light from a Picarro diode-pumped solid state laser for excitation in a backscattering geometry using the confocal microscope with a 100x objective on a Jobin-Yvon T64000 triple spectrometer operated in the subtractive mode. The incident laser light was focused on the LaS layer.

A. Prior experimental work

1. RE target preparation

In 2001, Cahay and co-workers reported the growth of a bulk sample of LaS using a two-step sesquisulfide route.[17] To grow the cubic phase of LaS, we first reacted equimolar portions of the rare-earth sesquisulfide, La_2S_3, and the rare-earth element, La, at 1800 °C for two hours in a high-temperature furnace from Thermal Technologies, Inc. A carbon reduction process during the high temperature annealing portion of the growth process was shown to greatly reduce the presence of oxysulfide impurity phases (La_2O_2S and Nd_2O_2S) in the samples. A picture of a LaS pellet prepared in a high-temperature induction furnace from Thermal Technologies, Inc., is shown in Fig. 3(a). Figure 3(b) shows an optical micrograph of a 30 μm^2 area inside a pellet showing a staircaselike growth pattern. Several of these pellets were prepared using the carbon reduction technique until enough material was produced to form a 2-inch diameter, 1/8-inch thick target, which was then sintered in the high-temperature furnace. The resulting target was then used for the PLD of LaS thin films. A comparison of the XRD spectra taken on a bulk LaS sample before and after the carbon reduction process is shown in Fig. 4.

2. PLD experiments

a. LaS/Si thin films. In the past, we reported the successful growth of nano-crystalline LaS thin films on Si (100) substrates by PLD at temperatures ranging from room temperature to 100 °C.[1,2] As shown in Fig. 5, these films are golden yellow in appearance with a mirrorlike surface morphology and a sheet resistance of around 0.1 Ω/square, as measured using a 4-probe measurement technique. For a
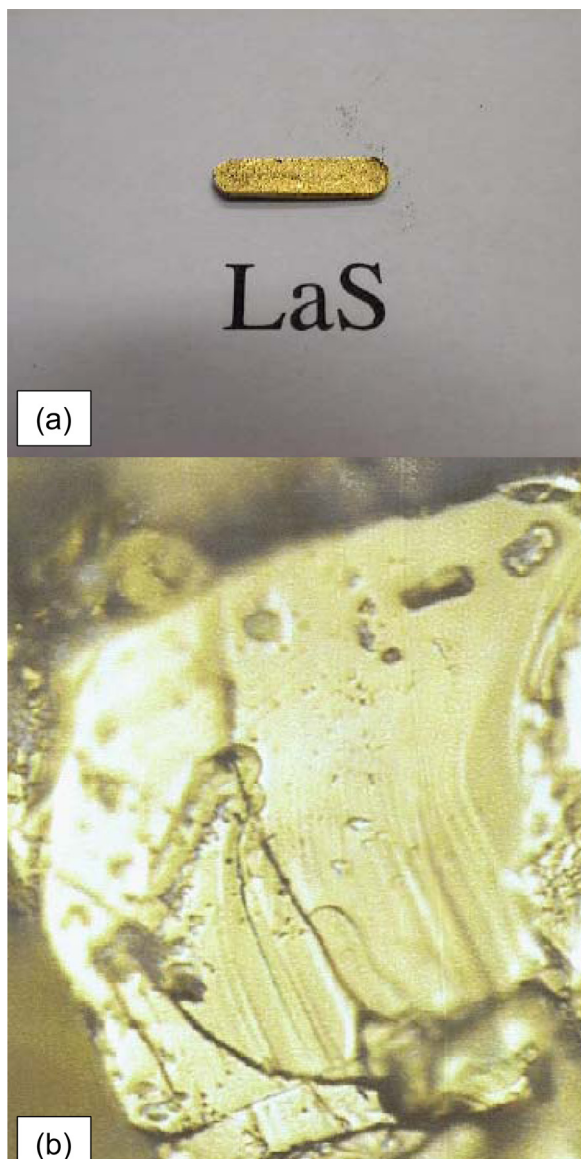
FIG. 3. (Color online) (a) Pellet of the cubic phase of LaS about 1.5 cm long, 4 mm wide and 2 mm thick prepared by the carbon reduction process. (b) Optical micrograph showing a large golden platelet (about 30 μm^2) of the cubic phase of LaS with a staircaselike growth pattern. [Reprinted with permission from M. Cahay, K. Garre, X. Wu, D. Poitras, D. J. Lockwood, and S. Fairchild, Journal of Applied Physics **99**, 123502 (2006).]

film grown at a repetition rate of 40 Hz with a substrate temperature of 100 °C and no background gas pressure, the growth rate was estimated to be about 20 nm/min. An AFM scan of this film over a 1 μm^2 area of a 1 micron thick film is shown in Fig. 6. The root-mean-square variation of the surface roughness over the 1 μm^2 area was found to be 1.74 nm. Figure 7 shows an XRD scan of this film revealing the successful growth of the cubic rocksalt structure with a lattice constant of 5.863(7) Å, which is close to the bulk LaS bulk value of a = 5.857(2) Å. The observation of many Bragg reflection peaks suggests that the film is polycrystalline, which is to be expected because of the large lattice mismatch (about 8%) between the lattice constant of the LaS rocksalt phase and of the Si substrate (a = 5.41 Å). In addi-
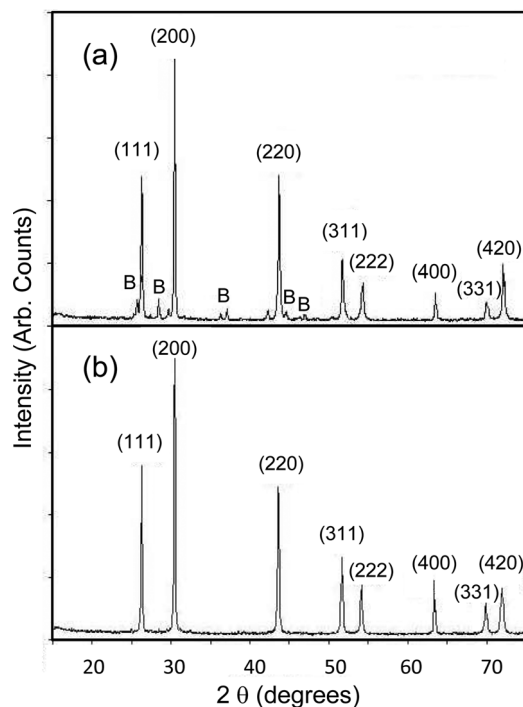

FIG. 4. Comparison of XRD scans of a LaS bulk sample (a) before, and (b) after the carbon reduction process. In the latter, the Bragg reflection peaks corresponding to the oxysulfide (La$_2$O$_2$S) impurity phase have disappeared.

tion, the Bragg peaks are very broad, suggesting the presence of polycrystalline grains of different sizes and potentially the presence of amorphous regions in the film. Using Scherrer's equation, the size of the nanocrystalline grains was found to be about 13 nm. This value agrees well with cross-section TEM analysis of the LaS films, as shown in Fig. 8. Extensive TEM analysis reveals the amorphous and crystalline regions comprised approximately 60 and 40% of the film, respectively.[1,2]

FIG. 5. (Color online) Thin film of LaS deposited by PLD on a square inch Si substrate. The reflection of the finger shows the metallic character of the thin film. [Reprinted with permission fromM. Cahay, K. Garre, X. Wu, D. Poitras, D. J. Lockwood, and S. Fairchild, Journal of Applied Physics **99**, 123502 (2006).])

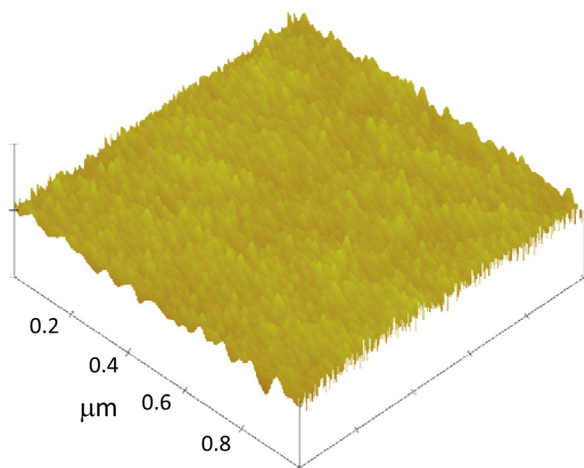FIG. 6. (Color online) AFM scans over a $1 \times 1 \, \mu m^2$ area of a LaS thin film (about one micron thick) grown on a (001) Si substrate The root mean square of the surface roughness is 1.74 nm over that area. [Reprinted with permission from M. Cahay, K. Garre, X. Wu, D. Poitras, D. J. Lockwood, and S. Fairchild, Journal of Applied Physics **99**, 123502 (2006).]

b. LaS/MgO thin films. LaS thin films were grown by PLD on (001) MgO substrates at an elevated substrate temperature and in a background gas of H_2S. The goal of this research was to prepare crystalline epitaxial films of LaS with (100) orientation capable of delivering higher emission current density than reported for the largely amorphous LaS/Si thin films. The approach is based on PLD at high temperature in a background gas of H_2S following the work of Piqué.[18,19] Single crystal MgO (001) with the NaCl structure was selected as the substrate of choice: MgO has a lattice constant of 4.213 Å. Cubic LaS has a lattice constant of 5.857 Å leading to a lattice mismatch of 1.69% when aligned with the unit cell diagonal of MgO (5.957 Å). It was found that a substrate temperature of at least 400 °C coupled with a low laser repetition rate and at least 20 mTorr of H_2S were
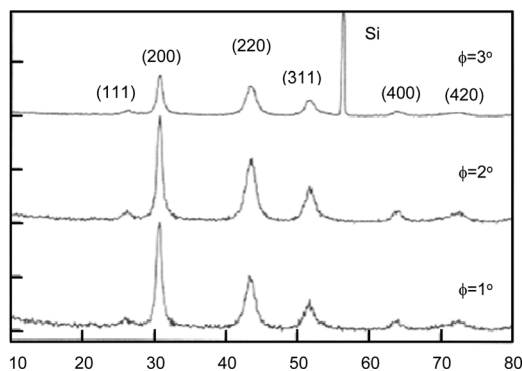

FIG. 7. X-ray diffraction pattern at three different grazing angles of incidence from a LaS thin film deposited on a (100) Si substrate. Miller indices (hkl) of the reflections from the cubic rocksalt phase of LaS are identified. The units along the horizontal axis are in degrees. The peak located around 56° is due to the (311) Bragg reflection observed for a bare Si substrate (Joint Committee on Powder Diffraction Standard card No. 77-211). [Reprinted with permission from S. Fairchild, J. Jones, M. Cahay, K. Garre, P. Draviam, P. Boolchand, X. Wu, and D. J. Lockwood, Journal of Vacuum Science and Technology B **23**, 318 (2005).]
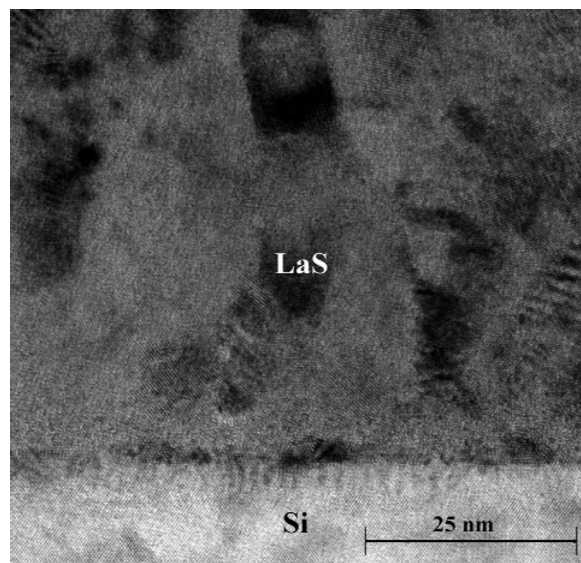
FIG. 8. High-resolution TEM image of the LaS/Si interface for a 1 μm thick LaS film grown on a (100) Si substrate. Despite the large lattice mismatch between the two materials (8%), the interface is rather at the length scale shown in this TEM picture. [Reprinted with permission from S. Fairchild, J. Jones, M. Cahay, K. Garre, P. Draviam, P. Boolchand, X. Wu, and D. J.Lockwood, Journal of Vacuum Science and Technology B **23**, 318 (2005).]

needed to produce crystalline cubic LaS as evidenced by XRD.[3] As shown in Fig. 9(a), for a LaS/MgO thin film grown at 400 °C in 24 mTorr of H_2S with a laser repetition rate of 4 Hz for 30 min, the film surface is composed of grainlike features with an average size of approximately 34 nm and the root-mean-square variation of the film surface roughness measured over a $2 \times 2 \, \mu m^2$ area by AFM was found to be about 1.5 nm. The XRD data indicate that the average size of the nanocrystalline grains in the film is about 26 nm, which is about twice the size of the grains found in LaS thin films deposited at room temperature on Si.

For comparison, Fig. 9(b) shows an AFM image of a LaS/Si sample over a $2 \times 2 \, \mu m^2$ area to 1.13 Å. The AFM scans demonstrate an abundance of grainlike features in the LaS/MgO thin films leading to enhanced field emission properties for these films. As discussed in the following text, the field emission (FE) properties of the LaS/MgO films have been characterized by the SAFEM technique and interpreted in terms of a patchwork FE model. The FE data indicate that there is roughly a 7 times increase in emission area due to (100) patch areas outcropping the surface for LaS/MgO films compared to LaS/Si thin films.

3. WF measurements

For UPS analysis, the LaS films were Ar etched at 1.5 keV for 120 s before data acquisition. The work function of the samples was determined by subtracting the width of the spectrum from the energy of the He I line (21.22 eV). The width of the spectrum was taken from zero binding energy (Fermi edge) to the onset of the secondary edge.[20] Figure 10 shows the UPS spectra of the LaS film. The sharp feature at low kinetic energy is the secondary edge cut-off.
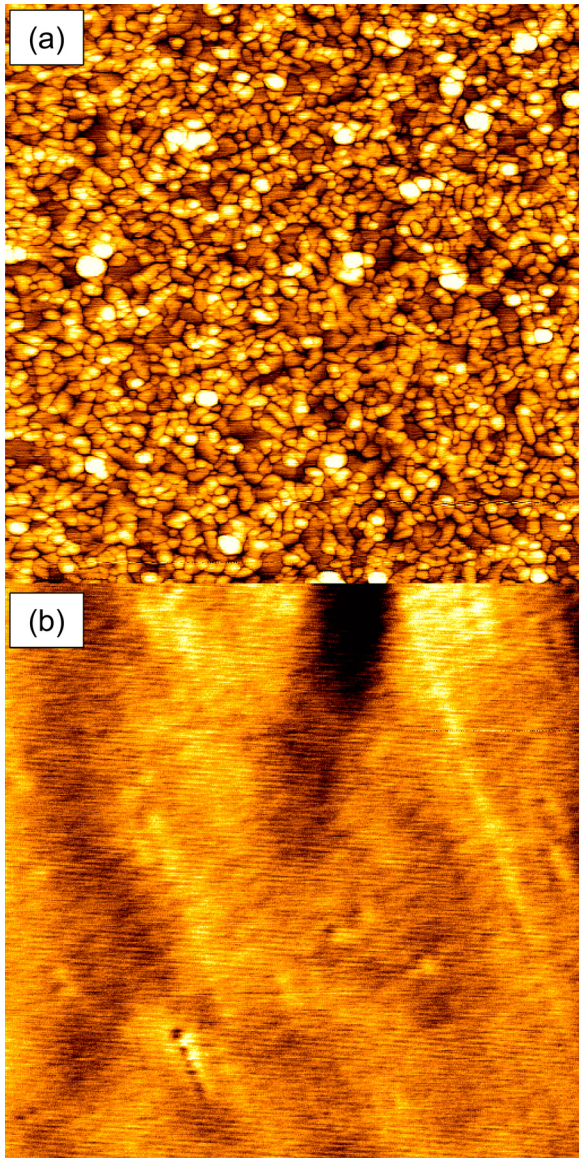
FIG. 9. (Color online) AFM scans over a $2 \times 2 \, \mu m^2$ area of (a) a LaS thin film grown on a (001) MgO substrate, and (b) a LaS thin film grown on a (100) Si substrate. The PLD parameters for both films were identical (substrate temperature: 400 C, 24 mTorr of H_2S background pressure, laser repetition rate of 4 Hz, deposition time: 30 min, substrate to target separation: 10 cm), except that the Si substrate was held at room temperature and no H_2S background gas was used during the growth. [Reprinted with permission from S. Fairchild, M. Cahay, L. Grazulis, K. Garre, J. W. Fraser, D. J. Lockwood, V. Semet, V. T. Binh, S. Bandyopadhyay, and B. Kanchibotla, Journal of Vacuum Science and Technology B **26**, 891 (2008).]

From this feature a work function of 2.9 eV was determined. The inset shows a magnified region around the Fermi energy. This value agrees well with the best work function of 2.6 eV recorded in air using a KP on a LaS pellet produced by an arc melting process.[21] For LaS/Si and LaS/MgO thin films, the WF values determined in air using a KP technique ranged from 3.7-4.7 eV.[22] These higher values are believed to be due to partial oxidation of the top surface of the film after exposure to air. Next, we compare these WF values to those extracted from the FE measurements using the SAFEM technique.
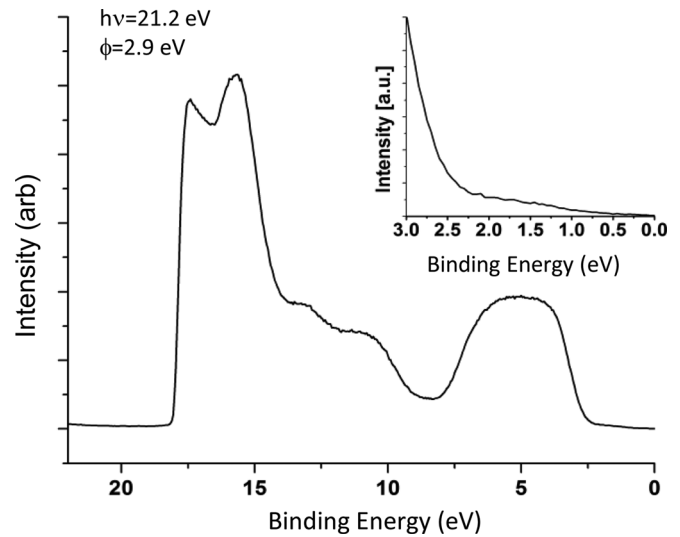
FIG. 10. UPS spectra of a LaS film deposited by pulsed laser ablation. The inset shows a magnified region at the Fermi energy (E_F).

4. SAFEM measurements

The main reason for surface instabilities and the breakdown of low work function cathodes (such as cesiated surfaces) results from a noncontrolled surface diffusion at the cathode surface induced by heating due to the field emission current. This thermal run-away process is amplified by the presence of adsorbates on the cathode surface. The RE monosulfide thin films, such as LaS/Si and LaS/MgO, in their rocksalt structure, offer a stable alternative as low work cathode material because of the patchwork nature of their field emitting surface, as will be discussed next.

To measure the field emission characteristic from LaS planar cathodes, we have scanned an anode probe located at micrometer distance over the cathode surface. Such an analytical device, called a scanning anode field emission microscope (SAFEM), has been fully described earlier.[15] The corresponding analytical procedure to extract, from the measured I-V data, the specific parameters of the cathode and in particular its surface barrier or work function have also been discussed in detail in Refs. 3, 4, and 24. The measurements have been done with different LaS planar cathodes, and the results were given in detail in recent articles where we studied field emission from LaS layers deposited on Si substrates,[1,2,23] LaS thin films grown on MgO substrates,[3] and LaS thin films deposited on self-assembled nanostructures.[4] Hereafter, we summarize the main findings:

(1) Stable and reversible field emission characteristics were obtained from a threshold of the applied electric field of ~230 V/μm and for current densities less than 0.3 and 7 A/cm^2, respectively, for Si and MgO substrates.

(2) The effective WF, ϕ_{eff}, of the LaS thin films was extracted from a Fowler-Nordheim analysis of the I-V characteristics in which the emitted current density, J, was computed using the transmission probability of an electron through the surface barrier outside the cathode. The corresponding Schrödinger equation was solved in its integral Lippman-Schwinger form by means of the
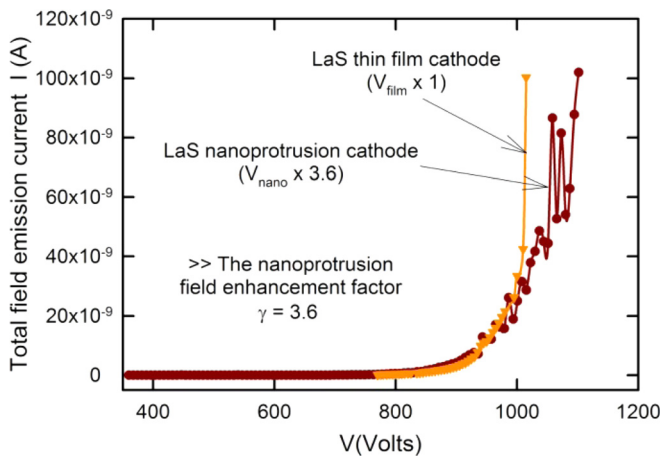
FIG. 11. (Color online) I-V characteristics for LaS thin film and nanoprotrusion cathodes. V_{film} and V_{nano} were the actual applied potentials to obtain field emission. The factor of 3.6 for nanoprotrusion means that one needs a potential that is 3.6 less than for a flat film to obtain the same field emission current. In other words, the field enhancement factor related to the nanodome geometry is at least 3.6.

FIG. 13. (Top) HRTEM image of the deposited LaS film showing the flat surface and the nanocrystalline nature of the layer. (Bottom) Schematic representation of a patchwork FE through nanocrystallites of a LaS thin film in close proximity of the probe ball (anode with a spherical shape) used in SAFEM experiments. The nanocrystallites (a) have a low work function (crystallites (a) and (b) have the same orientations), and the nanocrystallites (b) are not field emitting because they are embedded in the layer; the lines surrounding the nanocrystallites (a) schematically represent the current lines collecting the emitted electrons. [Reprint with permission from V. Semet, M. Cahay, V. T. Binh, S. Fairchild, X. Wu, and D. J. Lockwood, J. Vac. Sci. Technol. B **24**, 2412 (2006).]

Green's function technique. This approach allows for the inclusion of three emission mechanisms: thermionic, tunneling, and ballistic, all three being effective during field emission from cathodes with WF less than 2 eV. The technique is described in detail in Ref. 24. In the regime where $\ln(J/F^2)$ versus $1/F$ (where F is the externally applied electric field) shows a linear variation, the slope of the line is proportional to $(\phi_{eff})^3$ and was found to be in the range of 0.7 to 1 eV for LaS thin films grown on Si and MgO substrates.

(3) The comparison between a LaS flat film and layers with self-assembled nanodomes indicated a straightforward influence of the field enhancement factor, γ, of the nanoprotrusion (Fig. 11). Considering the geometry of the nanodomes, the value of 3.6 for the field enhancement is in good agreement with the well-known value of 3 for a hemisphere on a plane.[25]
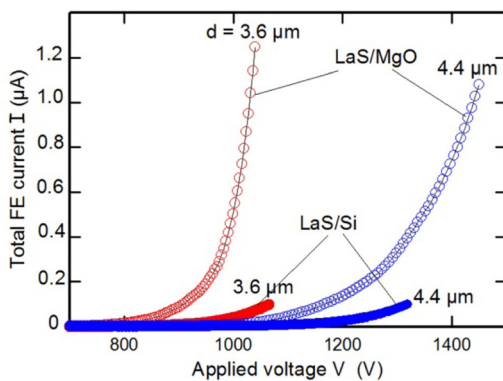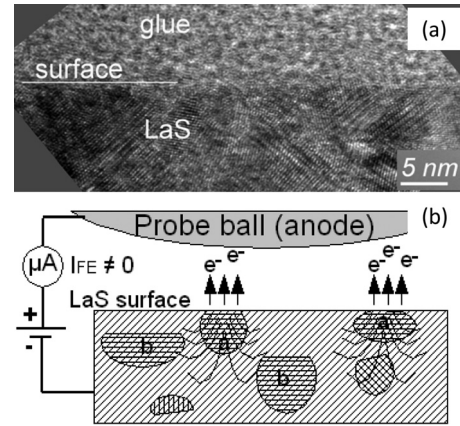

FIG. 12. (Color online) I-V characteristics for LaS deposited on MgO and Si. The two sets of data were obtained at the same probe distances, d, for the same field emission fields. [Reprinted with permission from S. Fairchild, M. Cahay, L. Grazulis, K. Garre, J. W. Fraser, D. J. Lockwood, V. Semet, V. T. Binh, S. Bandyopadhyay, and B. Kanchibotla, Journal of Vacuum Science and Technology B **26**, 891 (2008).]

(4) The comparison between LaS thin films deposited on Si and on MgO showed two main features. First, the surface barrier in both cases was the same and was on the order of 1 eV. Second, the field emission current for LaS on MgO was 7 times greater than for LaS on Si (Fig. 12). This specificity has to be placed in perspective with the areal density of the (100) oriented nanopatches which was found to be 7 time larger at the surface of the LaS/MgO thin films compared to those for the LaS/Si thin films. An HRTEM picture of the surface of a LaS/Si film is shown in Fig. 13(top) where nanopatches surrounded by amorphous material can clearly be seen. A schematic of the (100) oriented nanopatches outcropping the surface is shown in Fig. 13 (bottom).

(5) There was a limiting current beyond which the low surface barrier (1 eV) was destroyed. Beyond this threshold, further FE measurements gave an extracted value of 2.8 eV from the Fowler-Nordheim plot for the work function, in agreement with the Kelvin probe measurements.[23]

5. Patchwork field emission model

The analysis of the previously listed experimental results must explain the following characteristics:

(1) Why is there a difference in the WF values recorded with a Kelvin probe and those extracted from the SAFEM technique (2.8-3 eV compared to 1 eV, respectively)?

(2) The effective WF of 1 eV extracted from the SAFEM measurements was obtained without the need for extensive surface cleaning treatment, except for a gentle acetone rinse. Therefore, why did we observe a surface with

such a low barrier with apparently very little reaction with molecular species in the surrounding gases?

(3) What is the cause for the increase in the work function from 1 to 2.8 eV when the FE current goes through a threshold value?

Over the last few years, we have developed a patch-work FE model of LaS thin films.[26] Our analysis was based on the following two assumptions, resulting from the nanocrystalline structure of the LaS films previously described:

(1) The LaS nanocrystals presented low work function facets, on the order of 1 eV. This value is consistent with the (100) crystallographic orientation of LaS[6].
(2) Some of these (100) facets were outcropping the surface of the LaS thin films. These low WF nanocrystalline patches are surrounded by areas with an average WF of 2.8 eV.

The idea of patchwork field emission was first formulated by Herring and Nichols in 1949 to interpret the field emission from micron sized areas in thin film cathodes.[27] We have extended this model to the nanoscale region to explain the FE characteristics of LaS thin films. In Fig. 14(a), we show a schematic of a circular area representing the surface of a ⟨100⟩ oriented facet of a nanocrystal of LaS at the top of a thin film grown on a Si or MgO substrate, as shown in Fig. 13(a).

In our model, the ⟨100⟩ oriented nanocrystal is shown as a circular patch of radius, R, with a low work function ($\Phi_1 \sim 1$ eV) and surrounded by an amorphous phase with a larger work function, Φ_2 (2.8–3 eV). The latter value was determined using a Kelvin probe measurement of the work function. It is expected that the interface between the low and high work function regions is not abrupt, but extends over a contact zone of width, L_C, as shown in Fig. 14(a). At equilibrium, the Fermi level, E_f, in the patch and surrounding
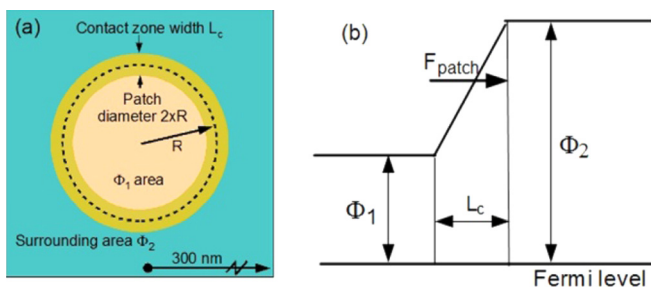
area must be aligned [see Fig. 14(b)]. Therefore, the potential energy profile along a line going from the center of the patch towards the outside in the plane of the LaS film must look as shown in Fig. 14(b). An estimate of the electric field, F_{patch}, over the patch is therefore given by,[15]

$$eF_{patch} = (\Phi_2 - \Phi_1)/R, \tag{1}$$

which is on the order of 10^7 V/cm.

With an anode placed on top of the thin film, the potential energy profile in the vacuum region was calculated by solving the Laplace equation within the zero emitted current approximation, i.e., assuming that no electron beam is injected from the patches with low work function. The energy potential contours are shown in Fig. 15 for different values of the applied electric field, F_{app}, across the vacuum gap.[23]

For low values of the applied electric field, the presence of the patch is hindered within a distance of a few nm from the surface by the electrostatic potential generated by the large work function surrounding area [Fig. 15(a)]. Practically, this suggests that work function measurements by field free macroscopic techniques, (i.e., Kelvin probe, UPS, thermionic, and photoemission measurements), operating with probe distances more than hundreds of nm away from the surface, cannot detect the presence of low work function patches if they are of nanometer sizes, typically on the order of 10 nm or less. This explains the discrepancy between our

FIG. 14. (Color online) (a) Schematic of a similar patch area with a low work function, Φ_1, and with a few nm diameter surrounded by a larger work function, Φ_2, amorphous phase. The separation between the two regions is not abrupt and the work function linearly increases from Φ_1 to Φ_2 over a connecting layer of width, L_C, around 0.5 nm. [Reprint with permission from V. T. Binh, R. Mouton, Ch. Adessi, V. Semet, M. Cahay, and S. Fairchild, J. Appl. Phys. **108**, 044311 (2010).] (b) Schematic of potential energy profile at equilibrium at the interface between the central patch with low work function, Φ_1, and the surrounding amorphous material with a larger work function, Φ_2.
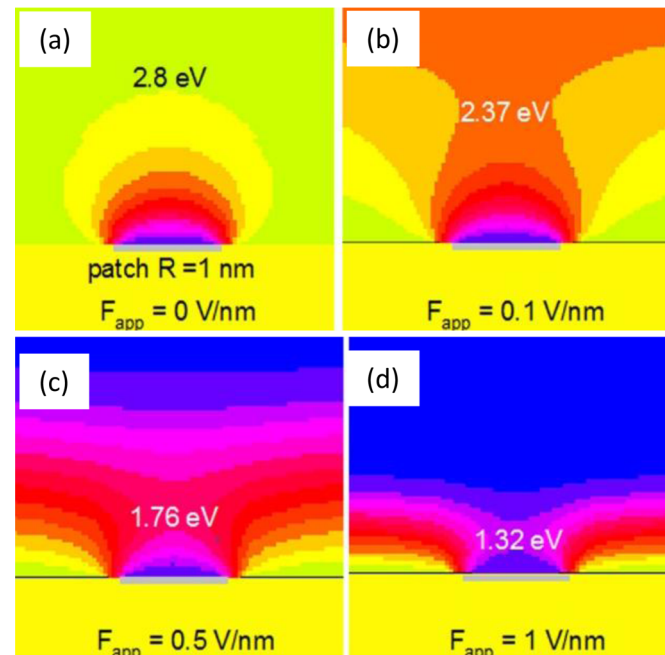

FIG. 15. (Color online) Evolution of the potential distribution over a 2 nm diameter patch showing the progressive opening over the patch for an increasing applied field, F_{app}. The patch has a WF of 1 eV and the surrounding medium has a WF of 2.8 eV. The data in the figures represent the lowest surface barrier height of the opening. In figure (d), for example, for an F_{app} of 1 V/nm the surface barrier height at the center of the patch is 1.32 eV. [Reprint with permission from V. T. Binh, R. Mouton, Ch. Adessi, V. Semet, M. Cahay, and S. Fairchild, J. Appl. Phys. **108**, 044311 (2010).]

work function measurements by the Kelvin probe and FE characteristics. Moreover, the potential screening of the low work function nanopatches by the surrounding high work function medium was sufficiently efficient to prevent strong surface chemical adsorption occurring on as-grown pristine LaS cathodes; therefore, allowing for the possibility to obtain FE without any prior thermal or sputtering treatments.

Eventually, the electrostatic opening of the patch occurs when the contribution of the externally applied field counterbalances the patch field estimated by Eq. (1), as shown in Fig. 15. Therefore, the potential distribution over the patch is dependent on the patch geometry, as illustrated in Fig. 16. This means that the FE from the patch cathode will be facilitated with an increase in the dimension of the patch, asymptotically reaching the classical behavior of two independent areas having, respectively, WFs of 1 and 2.8 eV. However, an increase in the patch dimension in order to increase the FE current must be balanced by the electrostatic potential protection of the patch by the high WF surrounding area in order to keep the patch surface free from adsorbates. This limits the size of the patch to an upper value of 100 nm.

From the progressive opening of the patch, the I-V characteristics from the patchwork cathode will first be governed by the progressive field emission from the patch until the beginning of the field emission from the surrounding region. Considering the difference in WF values between these two zones, the 1 eV patch region is largely in the ballistic regime before noticeable current can be extracted from the surrounding 2.8 eV WF surface. This is illustrated in Fig. 17, in which we have simultaneously plotted the I-V characteristics of the patchwork cathode, and the uniform surface cathodes of 1 and 2.8 eV WFs.

In Fig. 17, the saturation zone of the 1 eV cathode corresponds to the ballistic regime for field emission, i.e., the top
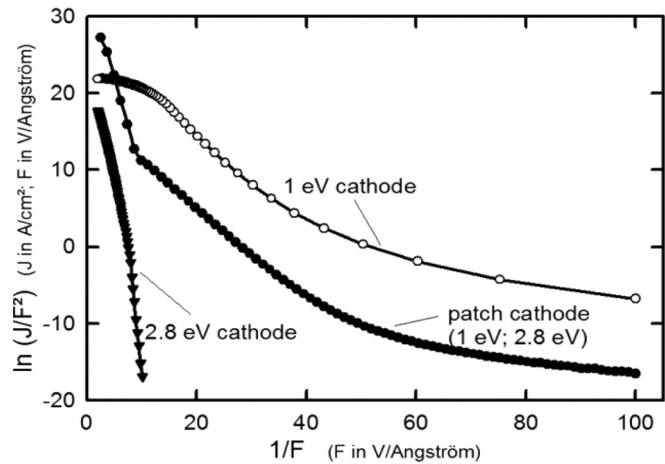

FIG. 17. Plots of I-V characteristics, respectively, for a patch cathode and for two uniform surface cathodes.

of the surface barrier is below the Fermi level. One can notice that before that ballistic threshold, the variation of the patch cathode is very comparable to the 1 eV cathode, thus proving that the emission current comes mainly from the patch area. Theoretically, when the 1 eV area reaches the ballistic regime the variation of the field emission current is then governed mainly by the FE current variation of the surrounding 2.8 eV area. This is illustrated in Fig. 17, where for $1/F < 10$ Å/V, the I-V plots for the patchwork cathode and the uniform 2.8 eV cathode have identical slopes. In an actual experiment, once the ballistic regime of operation is reached, the FE current density extracted from the patches can become so important that the patches can be destroyed by the local field emission induced thermal effect, resulting in a uniform 2.8 eV cathode.

We have conducted a preliminary study of the contribution of neighboring patches in a patchwork cathode.[26] It was shown that the global behavior of a patchwork cathode does not differ from a single patch cathode, as previously described, except for small modifications induced mainly by
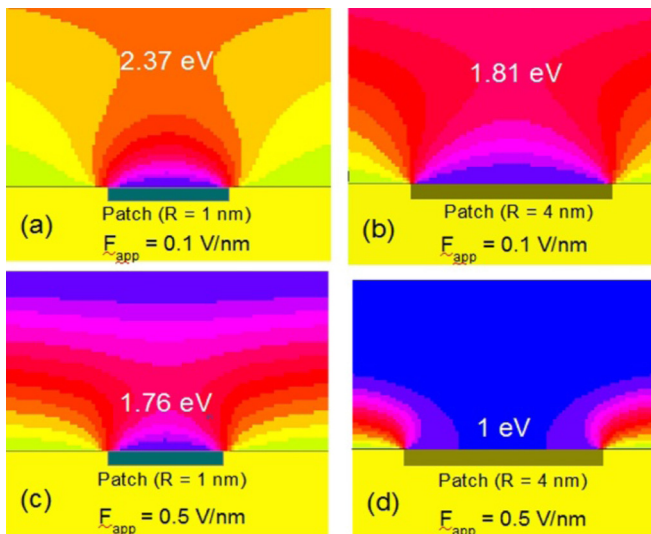

FIG. 16. (Color online) Potential opening over the patch for two patch dimensions (1 and 4 nm) and for the same applied fields (0.1 and 0.5 V/m).
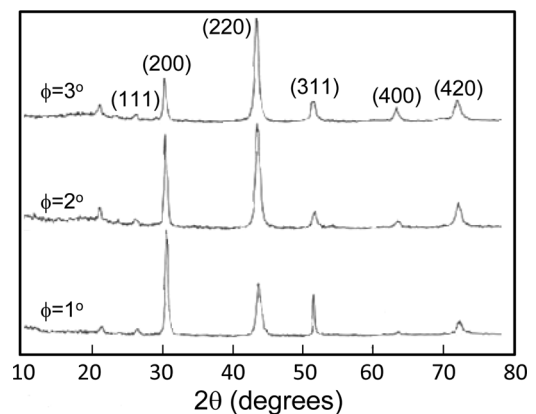

FIG. 18. X-ray diffraction pattern at three different grazing angles of incidence from a LaS thin film deposited on a (100) InP substrate. The units along the horizontal axis are in degrees. Miller indices (hkl) of the reflections from the cubic rocksalt phase of LaS are identified.

the coupling of the potential distribution between patches. The overall potential distribution over an array of patches keeps the same progressive barrier opening with the externally applied field above each individual patch. As a result, a nanopatchwork cathode will preferentially emit from an array of parallel e-beams strictly localized over the low WF patches. On a real polycrystalline surface, the patch distribution is more erratic. Therefore, more work is needed to gain control over the patch size and location to study the optimum conditions under which the low WF nanopatches stay protected from contamination by the surrounding material with a larger WF. A well regimented nanopatch structure would allow the emission of nondiffracted parallel nanosized e-beams with well-defined locations which would provide a new route for coherent parallel e-beam applications.

B. Recent experimental work

1. Growth of LaS thin films on InP substrates

The LaS thin films were grown by PLD on (100) oriented InP substrates at room temperature using the following PLD parameters: repetition rate = 4 Hz, laser energy = 850 mJ/pulse, and duration = 30 min. Figure 18 shows the x-ray diffraction pattern recorded at three different grazing angles of incidence. Miller indices (hkl) of the reflections from the cubic rocksalt phase of LaS are identified. The Bragg reflection peaks are narrower than those for a LaS thin film on a Si substrate, as shown in Fig. 7, indicating a much higher level of crystallinity in the Las/InP film due to the closer lattice-match between the two materials.

Figure 19 shows there are two LaS layers on the InP substrate, and the thicknesses of LaS(1) and LaS(2) are 52 and 121 nm, respectively. The surface and interface between LaS(1) and LaS(2) are flat in some areas [Fig. 20(a)], but undulated in other areas [Fig. 19(b)]. A (111) planar lattice defect indicated by a white arrow in Fig. 19(a) was observed in LaS(2). Selected area diffraction patterns from the LaS film [Fig. 19(c)] reveal that the LaS film has a polycrystalline nature.

Ellipsometric spectra, $\Psi(E)$ and $\Delta(E)$, measured from LaS on InP are shown in Figs. 20(a) and 20(b), respectively. Given the small size of the probed sample, the area of the incident beam used in ellipsometry had to be reduced, which may account for the large noise that is seen in the data, particularly in the UV part of the spectra where the signal was particularly weak. To extract the complex permittivity dispersion curves, $\varepsilon_1(E)$ and $\varepsilon_2(E)$ [shown in Fig. 20(c)], we attempted to fit the data using information from the TEM cross-section of the LaS film on InP (see Fig. 19); the model used for fitting is described in Table II, with a rough surface layer partially oxidized, and two different layers of LaS on InP. The dispersion curves of both LaS layers were based on a Drude-Lorentz type of oscillator,

$$\varepsilon = \varepsilon_\infty - \frac{A_D \Gamma_D}{E^2 + i\Gamma_D E} + \frac{A_L \Gamma_L}{E_L^2 - E^2 - i\Gamma_L E} = \varepsilon_1 - i\varepsilon_2. \quad (2)$$
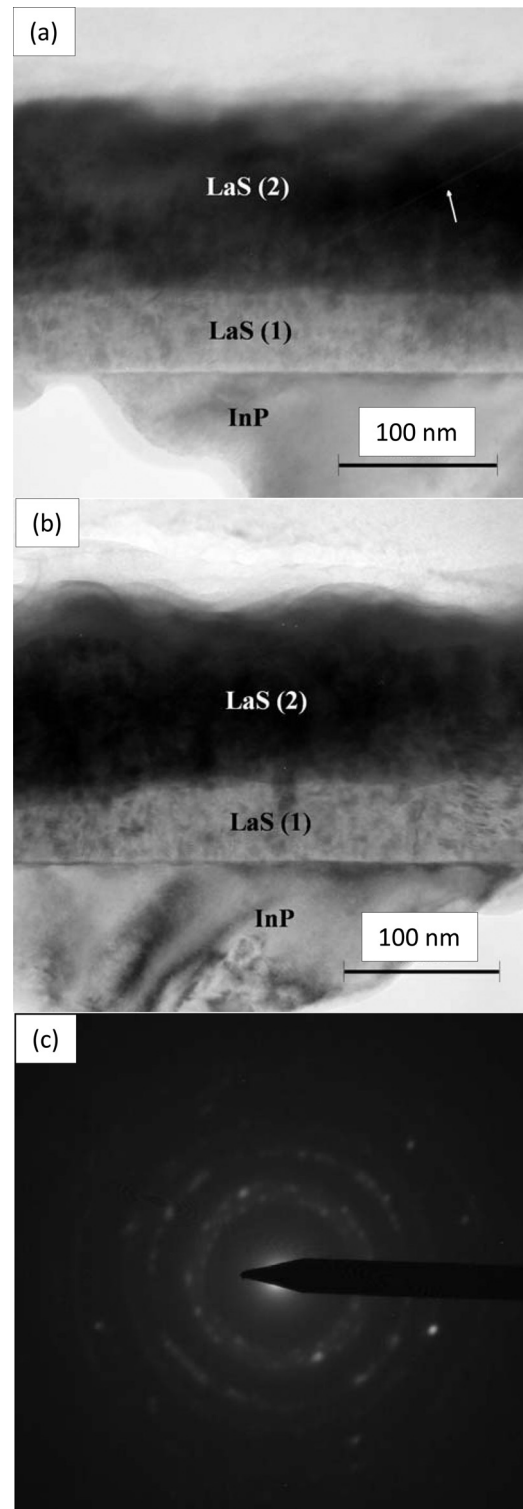
FIG. 19. (a) and (b) Cross-section TEM images of a LaS thin film on an InP substrate showing that there are two LaS layers on the InP substrate, and the thicknesses of LaS(1) and LaS(2) are 52 and 121 nm, respectively. (c) Selected area diffraction pattern from the LaS layers reveals that the LaS film has a poly-crystalline nature.

We found that: (i) a rough and oxidized surface layer of 35 nm was needed for the fitting (which is in good agreement with the TEM observations), while (ii) parameters from a bottom LaS layer had little influence on the fitting. The permittivity found for the 134 nm thick LaS layer is shown in
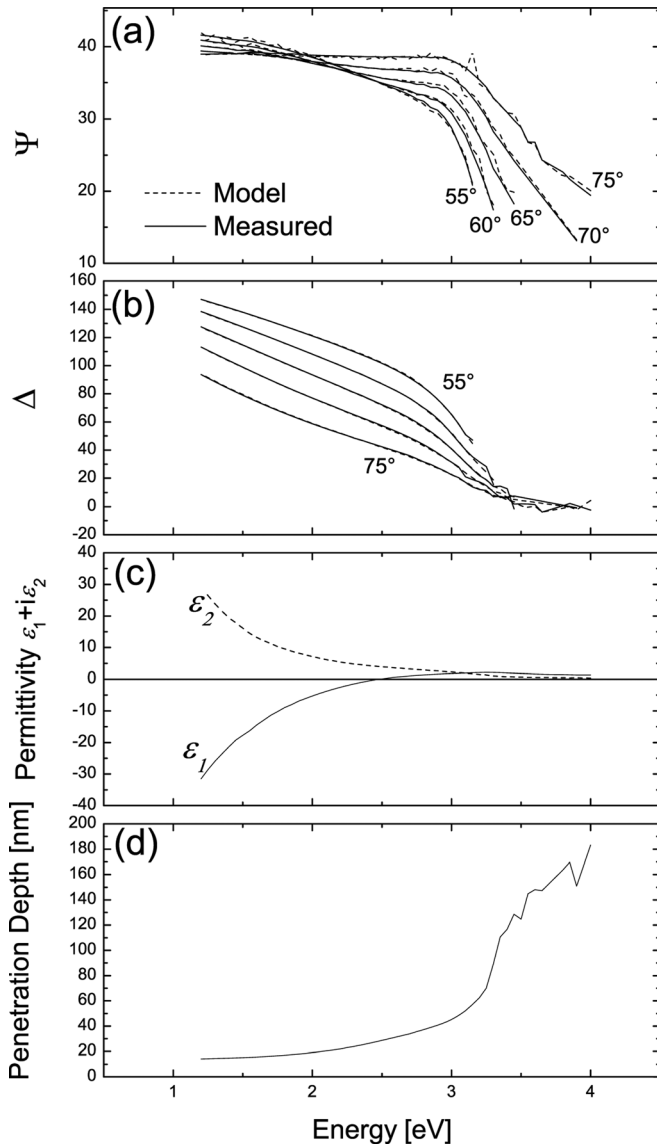
FIG. 20. (a) and (b) Ellipsometric spectra, $\Psi(E)$ and $\Delta(E)$, measured from LaS on InP, respectively. (c) The extracted complex permittivity dispersion curves, $\varepsilon_1(E)$ and $\varepsilon_2(E)$. (d) The estimated penetration depth of the light into the LaS film based on the permittivity dispersion.

TABLE II. Model used for fitting the ellipsometric data for a film of LaS on InP.

Layer	Description	Thickness
Top layer	Rough oxidized layer	35.4 nm
Layer 2	Top LaS layer	134.7 nm
Layer 1	Bottom LaS layer	52.0 nm
Layer 0	InP substrate	0.5 mm

The Raman spectra of the LaS/InP films exhibit weak broad features extending out to $600\,\mathrm{cm}^{-1}$, as illustrated in Fig. 21. Figure 20(d) shows that the Raman excitation light at 488 nm has a penetration depth of only 30 nm in the film. The results obtained are generally similar, but not in detail, to those found from Raman measurements on bulk pure LaS samples (see Fig. 21), confirming that the LaS films are of the pure cubic form. Strong peaks are observed at about 86 and $108\,\mathrm{cm}^{-1}$, with weaker features at 178, 198, 261, 301, 347, 448, and $518\,\mathrm{cm}^{-1}$.

One triply-degenerate optical phonon mode, split into longitudinal (LO) and transverse (TO) components, is expected for rare-earth monochalcogenides possessing the rocksalt crystal structure. First-order Raman scattering from phonons in such crystals is symmetry forbidden and usually a weak second-order Raman spectra is observed reflecting the two-phonon density of states (DOS). However, previous Raman studies of other rare earth chalcogenides[9,29] have shown that disorder introduced by defects such as cation and/or anion vacancies[9] can induce a first-order Raman spectrum reflecting the one-phonon DOS. The TEM analysis of our samples shows that structural disorder due to the formation of nanocrystals separated by amorphous material is also present. Thus, the Raman spectrum of our LaS films can be expected to show both disorder-induced first-order and

Fig. 20(c); the incident light energy value for which ε_1 equals zero (2.53 eV) corresponds to the plasma frequency below which the material starts behaving as a metal. Figure 20(d) shows the estimated penetration depth of the light into the LaS film based on the permittivity dispersion; it can be seen that below 3.5 eV, the light is not expected to reach the bottom LaS layer found on the TEM micrograph, which explains the small impact of this layer in our model, and is a typical metallic behavior.

Using a Drude model only [the first two terms of Eq. (2)], we re-fitted the portion of the data corresponding to the metallic region (energy values below the plasmon frequency), and estimated a carrier concentration and a mobility of $8.44 \times 10^{22}\,\mathrm{cm}^{-3}$ and $1.42\ \mathrm{cm^2\ V^{-1}\ s^{-1}}$, respectively (assuming an effective mass, $m^* = 1.3$) for the 134 nm thick LaS layer, and a resistivity of $5.22 \times 10^{-5}\ \Omega\,\mathrm{cm}^{-1}$ for that same layer.
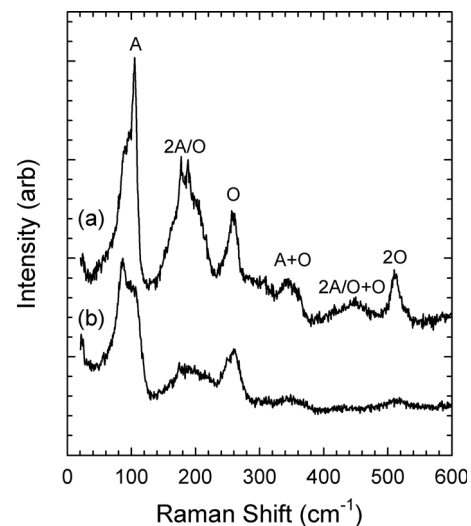

FIG. 21. Room temperature Raman spectrum of (a) bulk LaS (from a target similar to that used in the growth chamber) compared with (b) a LaS film grown on (100) InP. Here, A and O refer to acoustic and optical phonons involved in first-order and second-order Raman scattering.

second-order Raman features. In fact, our results for LaS films on InP resemble those previously obtained for LaS films on Si.[2] However, a closer examination of Fig. 21 shows that the Raman spectra of the present samples are quantitatively different from that of bulk LaS:[30] the Raman peaks above ~ 150 cm^{-1} are much weaker and more diffuse than those found in bulk LaS and no sharp features are seen at 106, 178, and 189 cm^{-1}. This is consistent with disorder in the LaS films.

The stronger features at 86 and 108 cm^{-1} are clearly due to disorder induced first-order Raman scattering from acoustic (A) phonons[2,9,29,30] while the peak at 261 cm^{-1} similarly arises from optic (O) phonons. Inelastic neutron scattering measurements of the acoustic phonon dispersion in LaS (Ref. 31) allow us to determine the origins of the acoustic Raman features. The 86 cm^{-1} peak arises primarily from transverse (TA) and longitudinal (LA) acoustic phonons at the X and K critical points in the Brillouin zone, while the shoulder at 108 cm^{-1} comes mainly from the L point TA and LA phonons. The distinct O peak at 261 cm^{-1} comprises contributions from both TO and LO phonons, with the highest frequency contributions from LO modes.[2] The broad and very weak bands occurring at frequencies higher than the optical phonon peak at 261 cm^{-1} are second-order in origin, primarily reflecting combinations of the disorder-induced first-order DOS Raman peaks. For example, the peaks at 347, 448, and 518 cm^{-1} can be attributed to the combinations of the 86 and 108 (A) cm^{-1} peaks with the 261 (O) cm^{-1} peak (A+O), 2 A/O+O and 2O, respectively (see Fig. 21).

2. Growth of LaS nanoballs and nanoclusters

Nanoclusters of LaS were fabricated by pulsed laser ablation (PLA) of a LaS target (5 cm diameter) with the output of a KrF ($\lambda = 248$ nm) excimer laser. The laser pulse duration was 25 ns, and the laser energy was 700 mJ per pulse. The target was rotated during deposition in order to expose a fresh LaS surface to each successive ablating laser pulse. Ablation was carried out in a static Ar background pressure of 1 Torr. Nanoclusters were deposited on a Si substrate (for SEM characterization) and on a TEM grid, both of which were situated 5 cm from the target. A total of four laser shots were used to fabricate the TEM samples, while the samples used for the SEM characterization were prepared by ablating the LaS target for 5 min at a repetition rate of 10 Hz.

Synthesis of nanoclusters by PLA typically results in a bimodal size distribution.[32] The smaller (1 nm < diameter < 10 nm) nanoclusters are formed by recombination in the gas phase of ablated atomic and molecular species. Larger nanoclusters are directly ejected from the target by a process denoted as splashing,[33] which can be understood by considering the nature of the species ejected from the target as a function of depth into the target. Species originating close to the target surface are exposed to the full laser energy and are ejected primarily as atoms; however, at great distances into the target, the laser energy is attenuated to such an extent that the target is heated rather than ablated. This results in the ejection of molten nanodroplets of liquid target material.

Although splashing can be an inconvenience for the deposition of epitaxial thin films, we use it to our advantage in nanocluster synthesis.

Presented in Figs. 22(top) and 22(bottom) are SEM micrographs of LaS nanoclusters formed by PLA. The nanocluster seen in Fig. 22(top) is spherical and has a diameter on the order of 300 nm. The spherical nature of the nanocluster, and its fairly large diameter, implies that this species was directly ejected from the target by splashing. The spherical nature of the feature also suggests that the particle was in the liquid state during part of its journey from target to substrate. Although it is difficult to discern from this single SEM image, it is observed quite often that these hot liquid nanodroplets become flattened as they strike the substrate such that their height (above the substrate) is less than their diameter. Such characteristics are more easily seen by AFM analysis.

Shown in Fig. 22(bottom) is an agglomeration of LaS nanoclusters that range in size from ~ 60 to 200 nm. It is interesting to note that the smaller nanoclusters tend to have spherical shapes and appear to have fused slightly with their adjacent nanoclusters (again consistent with their being ejected as liquid nanodroplets). It is also interesting to note that the larger nanoclusters appear to have more angular features, possibly suggesting that they were ejected from the target with temperatures that were insufficient to cause melting. Shown in Fig. 23 is a XRD Θ-2Θ scan of LaS nanoclusters deposited on Si. The broad peaks around 30° and 44° are assigned to be,
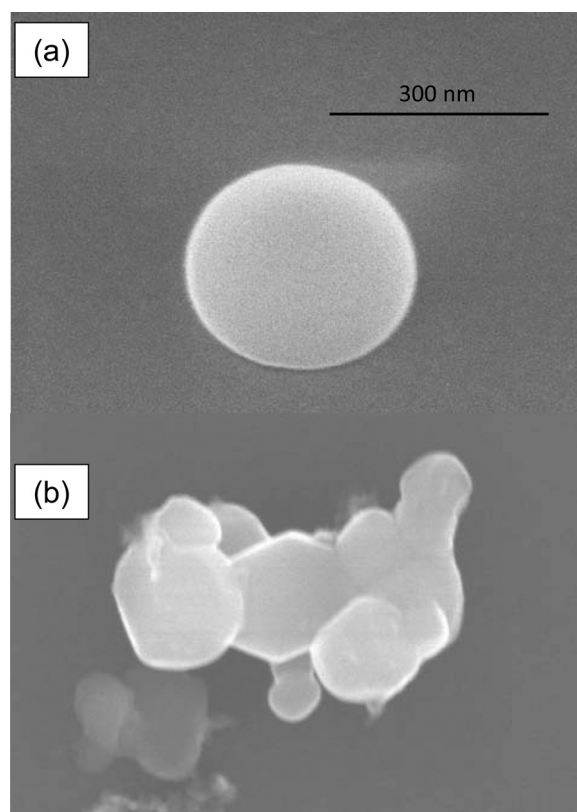

FIG. 22. FE-SEM images of (a) a single, and (b) a cluster of LaS nanoballs grown on a Si substrate using the following PLA parameters: 248 nm excimer laser, laser pulse duration = 25 ns, 700 mJ/pulse, 10 Hz, 5 min deposition, 1 Torr Ar background pressure, target to substrate separation, 5 cm.
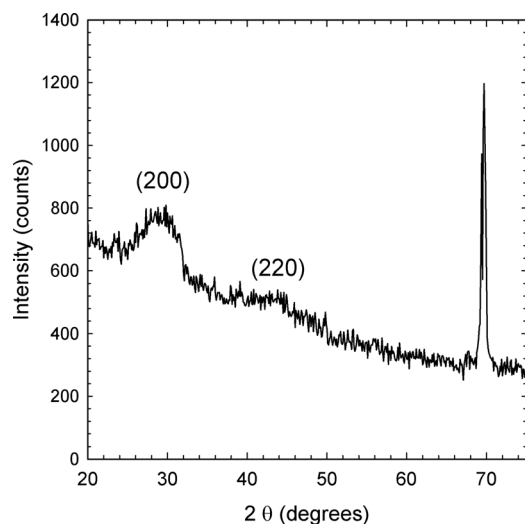
FIG. 23. XRD Θ-2Θ scan of LaS nanoclusters deposited by PLA on a Si substrate.

respectively, the (200) and (220) Bragg reflections of the cubic phase of LaS. The peak broadness is due to the large variation in size of the nanoclusters. The sharp peak around 70° corresponds to the (400) reflection of the Si susbtrate.
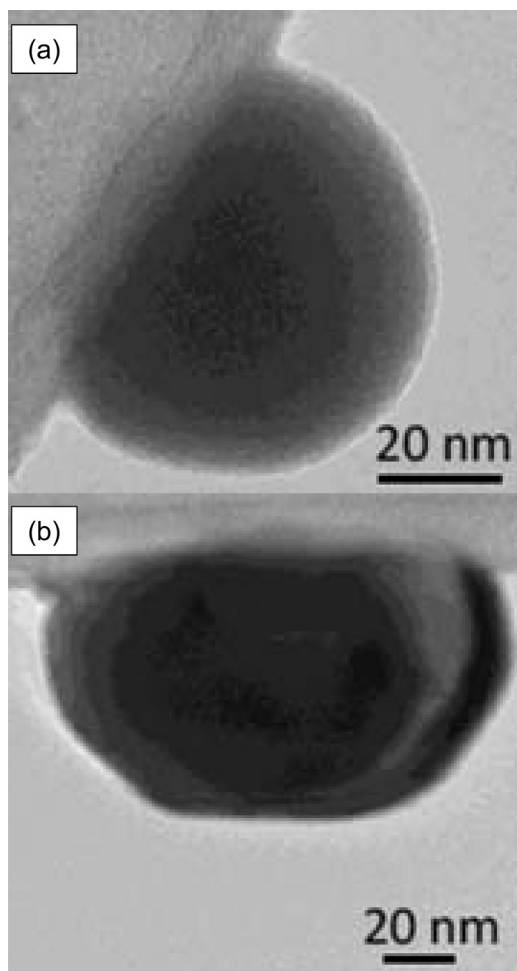

FIG. 24. TEM micrographs of single LaS nanoparticle deposited on a TEM grid. The PLA parameters were: 248 nm excimer laser, laser pulse duration 25 ns, 700 mJ/pulse, 4 pulses, 1 Torr Ar background pressure, target to substrate separation, 5 cm.

The TEM micrographs of LaS nanoclusters are shown in Fig. 24. The nanocluster seen in the left image has a diameter of ∼60 nm and has a spherical shape which is partially obscured by the support grid on the left side of the nanocluster. The spherical shape suggests that this object was liquid during its journey from target to substrate. Shown on the right side of Fig. 24 is a nanocluster that presumably flattened upon impact with the TEM grid. It is interesting to note that this nanocluster has some angular features, which suggests the possibility that the nanocluster had undergone partial crystallization upon impact.

III. CONCLUSIONS

Typically, low work function surfaces are generally highly chemically reactive. As a result, cold cathodes made of these materials are very unstable. During the last ten years, we have developed a new class of field emitters based on rare-earth monosulfide thin films which turned out to be very reliable and durable. In fact, rare-earth monosulfides are unusual in many respects; not only do they possess high chemical stability (melting temperatures above 2000 °C), but they also display metallic conduction. So far, LaS thin films have been successfully grown using PLD on Si and InP substrates at room temperature and on MgO substrates at high temperature in the presence of a H_2S background gas.

LaS/MgO thin films were used successfully as cold cathode emitters with measured emitted current densities as high as 50 A/cm^2. For both LaS/Si and LaS/MgO thin films, the effective work function of the micron sized thin films was determined from field emission measurements using the scanning anode field emission microscopy (SAFEM) technique. From the Fowler-Nordheim plots of the field emission characteristics of the thin films, an effective work function around 1 eV was extracted. The physical reasons for these highly desirable low work function properties were explained using a patchwork field emission (FE) model of the emitting surface in which nanocrystals of low work function materials having a $\langle 100 \rangle$ orientation perpendicular to the surface and outcropping it are surrounded by a matrix of amorphous materials with a higher work function.[27]

Recent numerical calculations of the patch-field distribution across these nanopatchwork surfaces show that low work function nanosize zones (with diameter less than a few tens of nm) are intrinsically protected by an electrostatic screen induced by the surrounding media with a higher work function. The latter prevents molecules from absorbing onto the lower function areas, protecting them from contamination until a bias applied to an anode in close proximity opens up channels for efficient field emission on top of the 1 eV nanocrystals. Therefore, the nanopatch structure allows the emission of nondiffracted parallel nanosize electron (e-) beams with well-defined spatial locations. The production of a high density array of these parallel e-beams is, therefore, no longer hindered by the presence of physical electrodes (such as extracting lenses and diaphragms) in the very near neighborhood of a tip configuration cathode surface, as in current e-beam systems. With the patchwork cathode, the structure of the e-beam array and its resolution are

only determined by the location and dimension of the nano-patches over a plane surface, opening a new route for coherent parallel e-beam applications.

More recently, we have been able to produce LaS nano-balls and nanoclusters by PLA. The latter can be used to control the density and size of the nanopatches to generate a high density of parallel nanosize electron-beams.

ACKNOWLEDGMENTS

[1]S. Fairchild, J. Jones, M. Cahay, K. Garre, P. Draviam, P. Boolchand, X. Wu, and D. J. Lockwood, J. Vac. Sci. Technol. B **23**, 318 (2005).

[2]M. Cahay, K. Garre, X. Wu, D. Poitras, D. J. Lockwood, and S. Fairchild, J. Appl. Phys. **99**, 123502 (2006).

[3]S. Fairchild, M. Cahay, L. Grazulis, K. Garre, J. W. Fraser, D. J. Lockwood, V. Semet, V. T. Binh, S. Bandyopadhyay, and B. Kanchibotla, J. Vac. Sci. Technol. B **26**, 891 (2008).

[4]M. Cahay, K. Garre, V. Semet, V. T. Binh, J. W. Fraser, D. J. Lockwood, S. Bandyopadhyay, S. Pramanik, B. Kanchibotla, S. Fairchild, and L. Grazulis, J. Vac. Sci. Technol. B **25**, 594 (2007).

[5]The room-temperature work function for RE monosulfides listed in Table I was calculated by extrapolating measured work function values at high temperature as reported by S. Fomenko, in *Handbook of Thermionic Properties* (Plenum, New York, 1966). For RE monosulfides, the work function increased with temperature at a rate of a few meV/K.

[6]O. Eriksson, J. Willis, P. D. Mumford, M. Cahay, and W. Friz, Phys. Rev. B **57**, 4067 (1998).

[7]O. Eriksson, M. Cahay, and J. Wills, Phys. Rev. B **65**, 033304 (2002).

[8]O. Eriksson, M. Cahay, and J. Wills, "Negative electron affinity material: NdS on GaAs," (unpublished).

[9]W. Friz, Final Technical Report: "Dynamic work function shift in current carrying thin films," Task ELM-9, June 1992; Technical Note: "Cold Electron Emitters," Task ELM-6, January 1995; Progress Report: "More on Cold Electron Emitters," Task ELM-11, June 1995, Wright-Patterson Air Force Base.

[10]P. D. Mumford and M. Cahay, J. Appl. Phys. **79**, 2176 (1996).

[11]P. D. Mumford and M. Cahay, J. Appl. Phys. **81**, 3707 (1997).

[12]Y. Modukuru and M. Cahay, J. Vac. Sci. Technol. B **19**, 2149 (2001).

[13]A. Malhotra, Y. Modukuru, and M. Cahay, J. Vac. Sci. Technol. B **16**, 3086 (1998).

[14]C. Hammond, *The Basics of Crystallography Diffraction* (Oxford University Press, New York, 2003).

[15]V. Semet, R. Mouton, and V. T. Binh, J. Vac. Sci. Technol. B **23**, 671 (2005).

[16]V. Semet, Ch. Adessi, T. Capron, and V. T. Binh, Phys. Rev B **75**, 045430 (2007).

[17]Y. Modukuru, J. Thachery, H. Tang, A. Malhotra, M. Cahay, and P. Boolchand, J. Vac. Sci. Technol. B **19**, 1958 (2001).

[18]A. Piqué, M. Mathur, J. Moses, and S. A. Mathews, Appl. Phys. Lett. **69**, 391 (1996).

[19]A. Piqué, R. C. Auyeung, S. B. Qadri, H. Kim, B. L. Justus, and A. L. Huston, Thin Solid Films **377-378**, 803 (2000).

[20]S. Hüfner, *Photoelectron Spectroscopy* (Springer, Berlin, 1995).

[21]Y. Modukuru, J. Thachery, H. Tang, M. Cahay, and P. Boolchand, "Synthesis and Work Function Measurement of LaS and NdS bulk samples," in Proceedings of the First International Symposium on Cold Cathodes, 198th Meeting of the Electrochemical Society, Phoenix, AZ, October 2000.

[22]S. Fairchild, "Pulsed laser deposition of lanthanum monosulfide thin films for cathode material applications," Ph.D thesis, University of Dayton, 1997.

[23]V. Semet, M. Cahay, V. T. Binh, S. Fairchild, X. Wu, and D. J. Lockwood, J. Vac. Sci. Technol. B **24**, 2412 (2006).

[24]C. Adessi and M. Devel, Ultramicroscopy **85**, 215 (2000).

[25]D. J. Rose, J. Appl. Phys. **27**, 215 (1956).

[26]V. T. Binh, R. Mouton, Ch. Adessi, V. Semet, M. Cahay, and S. Fairchild, J. Appl. Phys. **108**, 044311 (2010).

[27]C. Herring and M. H. Nichols, Rev. Mod. Phys. **21**, 185 (1949).

[28]G. Güntherodt, P. Grünberg, E. Anastassakis, M. Cardona, H. Hackfort, and W. Zinn, Phys. Rev. B **16**, 3504 (1977).

[29]A. Treindl and P. Wachter, Phys. Lett. A **64**, 147 (1977).

[30]I. Frankowski and P. Watcher, Solid State Commun. **40**, 885 (1981).

[31]M. M. Steiner, H. Eschrig, and R. Monnier, Phys. Rev. B **45**, 7183 (1992); W. Reichardt (unpublished).

[32]J. F. Ready, Appl. Phys. Lett. **3**,11(1963).

[33]P. T. Murray and E. Shin, Proc. SPIE **7404**, 74040F (2009).